ADVANCED ENGINEERING MATERIALS
www.aem-journal.com

Electric Current-Assisted Sintering of 8YSZ: A Comparative Study of Ultrafast High-Temperature Sintering and Flash Sintering

Shufan Wang, Tarini Prasad Mishra, Yuanbin Deng, Luca Balice, Anke Kaletsch, Martin Bram, and Christoph Broeckmann*

Electric current-assisted sintering (ECAS) is a promising powder consolidation technique that can achieve short-term sintering with high heating rates. Currently, main methods of performing ECAS are indirect heating of the powder compact in a conductive tool or direct heating with current flowing through the powder compact. Various influencing factors have been identified to explain the rapid densification during ECAS, such as ultrahigh heating rates, extra-high temperatures, and electric field. However, the key consolidation-enhancing factor is still under debate. This study aims at understanding the role of heating rate on the enhanced densification during ECAS of 8 mol% Y_2O_3-stabilized ZrO_2 (8YSZ) by experimental and numerical methods. Two different heating modes, ultrafast high-temperature sintering (UHS, indirect heating) and flash sintering (FS, direct heating), are studied. The novel UHS technique is successfully applied to consolidate the 8YSZ samples. Additionally, finite element methods (FEM) combined with a constitutive model is adopted to predict the densification and grain growth. Furthermore, a comparison of UHS and FS is performed to investigate the thermal effect (heating rate) and athermal effect (electric field) individually. The results indicate that the high heating rate is the key factor of the rapid densification during UHS and FS of 8YSZ.

1. Introduction

The sintering of ceramic materials normally requires high energy consumption and long processing times. For traditional sintering techniques, such as free sintering in conventional furnaces, high temperatures up to 2000 °C and long dwell times for several hours are commonly used for producing ceramic materials. However, as these energy-intensive processes have a strong negative environmental impact, novel sintering techniques with higher energy efficiency are highly demanded. Promising approaches are the use of additional process control parameters like pressure,[1–3] sintering aids,[4,5] and electric field.[6,7] Besides the low furnace temperature and reduced sintering time, these techniques bring auxiliary benefits including fine grain size[8,9] and improved mechanical properties.[10]

Electric current-assisted sintering (ECAS) techniques have attracted considerable attentions over the last few decades. ECAS is a class of consolidation methods in which the application of an electric field allows an ultrahigh heating rate and a significant reduction in sintering time.[11–13] The rapid heating and enhanced densification during ECAS can be achieved either by direct heating of conductive ceramics by the Joule effect or by indirect heating of nonconductive powders in a conductive tool. Field-assisted sintering technology/spark plasma sintering (FAST/SPS)[14,15] can densify both conductive and nonconductive powders with the help of a conductive tool and external pressure. Flash sintering (FS)[16,17] utilizes thermal radiation to heat the nonconductive samples to an onset temperature, where current starts to flow through the sample with a thermal runaway effect. Recently, a new sintering technology called

S. Wang, Y. Deng, A. Kaletsch, C. Broeckmann
Institute of Applied Powder Metallurgy and Ceramics at RWTH Aachen e.V. (IAPK)
Augustinerbach 4, 52062 Aachen, Germany
E-mail: s.wang@iwm.rwth-aachen.de

The ORCID identification number(s) for the author(s) of this article can be found under https://doi.org/10.1002/adem.202300145.

DOI: 10.1002/adem.202300145

T. P. Mishra, L. Balice, M. Bram
Institute of Energy and Climate Research: Materials Synthesis and Processing (IEK-1)
Forschungszentrum Jülich GmbH
52425 Jülich, Germany

Y. Deng, A. Kaletsch, C. Broeckmann
Institute for Materials Applications in Mechanical Engineering (IWM)
RWTH Aachen University
Augustinerbach 4, 52062 Aachen, Germany

M. Bram
Institut für Werkstoffe
Ruhr-Universität Bochum
Universitätsstraße 150, 44801 Bochum, Germany

ultrafast high-temperature sintering (UHS) was reported by Wang et al.[18] In their study, two carbon strips were connected to the electrodes and heated by Joule heating, and the powder compact was placed between the strips and heated by radiation and conduction. It was found that the ceramic powder compacts were able to be consolidated in a few seconds or minutes.[18–20] It was also reported that the heating rate in UHS can reach 10^3–10^4 K min^{-1} which could significantly lower the apparent activation energy for densification.[18,21] Ultrahigh heating rate is believed to be able to suppress the grain growth due to the very short time the sample is at high temperature.[22] As coarsening changes the local surface curvature and thus decreases the driving force for sintering, the fine grain sizes can facilitate the densification during sintering. Furthermore, high heating rate allows bypassing the surface diffusion stage which does not contribute to consolidation, and thus enhance the densification and shorten the sintering time.[23,24] Therefore, the key factor of the rapid densification during ECAS was attributed to the high heating rate by many researchers.[25–28] However, other studies suggested that the effect of electric field in FS and the extremely high maximum temperature of the sample also play a role in the enhanced densification.[29,30]

To study the temperature profile of the ceramic sample for investigating the densification mechanisms during ECAS, modeling efforts have been made both on FS[31–34] and UHS[8,9,26,35] in recent years. Mishra et al.[26] adopted finite element methods (FEM) to simulate the temperature distribution in strontium titanite (STO) during UHS and found that the temperature required to densify the ceramic green body by UHS is comparable to that by conventional sintering (CS). Dong et al.[9] used the master sintering curve (MSC) approach combined with FEM to predict the densification of 3 mol% yttria-stabilized zirconia (3YSZ) during a thermally insulated UHS. In their study, the apparent activation energy for densification was fitted as 680 kJ mol^{-1}, which is similar to the literature values of 3YSZ. Therefore, they concluded that the previously claimed notable heating rate effect on the activation energy for sintering is not valid. However, the UHS experiments in their study were carried out in argon atmosphere, whereas the CS experiments of 3YSZ were conducted in air. It was reported that the densification of 3YSZ during sintering in argon is harder than in air,[36] but a clear explanation of this experimental finding is not given. Considering the possible influence of the sintering atmosphere on the activation energy for densification, the aforementioned conclusion of no significant heating rate effect on the activation energy is not convincible.

In this work, the densification and grain growth kinetics during UHS of 8 mol% Y_2O_3-stabilized ZrO_2 (8YSZ) were studied both experimentally and numerically. As no current flows through the sample during UHS, it has the advantage over FS of excluding the athermal effect (electric field) and investigating only the influence of heating rate on densification. A comparison of the sintering behaviors of 8YSZ during UHS and FS was then performed to study the role of heating rate and electric field on the rapid densification. The study of FS of 8YSZ was reported in our previous work.[37]

2. Experimental Procedures

2.1. Specimen Preparation

For all UHS and FS experiments, 8YSZ powder produced by Tosoh Corporation with an average particle size of 0.18 μm was employed. The starting powder was uniaxially pressed into pellet-shaped powder compacts with a pressure of 100 MPa for UHS experiments. The samples had a diameter of 8 mm and a thickness of 1–1.2 mm. Afterward the powder compacts were presintered in a furnace at the temperature of 1000 °C for 60 min to avoid the formation of entrapped gases during UHS. For FS, dog bone-shaped samples were produced by uniaxial pressing at 100 MPa. The samples have a gauge length of 15 mm, a width of 3.3 mm, and a thickness of 1.8–2.1 mm. Subsequently, a presintering at 900 °C for 60 min was carried out on the green bodies. The detailed description of the specimen preparation and experimental procedures of FS was reported in another study[37] and is not repeated in this article. A starting relative density (RD) of 45% ± 2% was determined on the presintered powder compacts for both UHS and FS.

2.2. Sintering Experiments

The UHS setup was custom-made and consists of two copper electrodes and a carbon felt (40 mm × 9.5 mm × 4 mm). A 9 mm length slit was cut in the middle of the carbon felt, and the 8YSZ pellet-shaped powder compact was put in the center of the felt. A good contact between the electrode and the felt was ensured by tightening the screws on the electrodes to allow the current to flow through the carbon felt. The schematic diagram of the setup is illustrated in the work of Mishra et al.[26] and shown in **Figure 1**a. The setup was operated in a chamber filled with argon

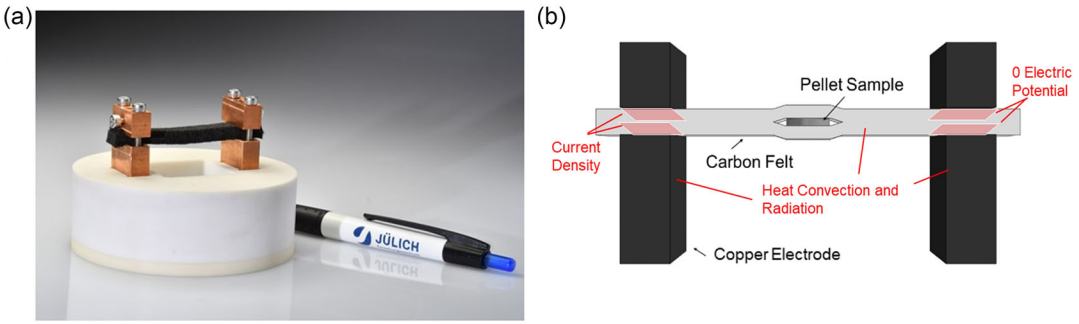

Figure 1. a) Experimental setup of UHS; b) simulation model of the UHS setup with defined boundary conditions.

to prevent oxidation of the carbon felt. An AC/DC power source (TruPlasma Bipolar Series 4000, Trumpf Hüttinger) was used to produce the electric current. After the chamber was evacuated (<0.2 mbar), it was filled with argon at a constant gas flow of 10 L min^{-1}. Subsequently, a DC electric current of 10–13 A with 1 A interval was applied to the carbon felt by metallic copper electrodes. The Joule heating induced fast heating of the carbon felt, and the sample was heated by thermal conduction and radiation. After the current reached the desired values, it was held for four different dwell times of 30, 60, 90, and 120 s. Those 16 interrupted isothermal experiments were used for parameter identification for the sintering model. An additional experiment with a current of 15 A and a dwell time of 30 s was performed to study the sintering behavior at high current level. Finally, the power source was switched off and the chamber was evacuated again to remove the argon. After cooling, the sintered samples were taken out of the carbon felt and their densities were measured by the Archimedes method. During the experiments, the sample temperature could not be measured adequately due to the ultrahigh heating rates. As discussed in more detail later, heating rates of 8YSZ samples in the case of UHS experiments were in the range of 2000–3000 K min^{-1} depending on the current level. However, a pyrometer was used to measure the highest temperatures reached on the top surface of the carbon felt. Furthermore, in a previous work,[26] a thermal couple, nickel-chromium wires, and platinum wires were used to determine the highest temperatures of the inner surface of the carbon felt at different currents. The measurements above help us to verify the simulation results of the temperature distribution in the carbon felt, thus allowing us to estimate the sample temperatures.

For comparison, CS experiments were also carried out in a push rod dilatometer TMA 402 F1 (Netzsch, Germany). The cylinder-shaped samples with a diameter of 8 mm were sintered in argon atmosphere to keep the consistency with the UHS experiments. For all dilatometer experiments, a heating rate of 5 K min^{-1} was applied. Different sintering cycles were used for the conventional experiments. The processing parameters of dilatometer sintering as well as the UHS are summarized in **Table 1**. For UHS, the average temperatures of the sample are estimated to be 1100–1500 °C for the given currents (10–15 A) and dwell times according to the simulation.

Table 1. Summary of experimental parameters for the sintering experiments.

Experiment	Sintering condition	Dwell time
UHS	10 A	30, 60, 90, 120 s
	11 A	30, 60, 90, 120 s
	12 A	30, 60, 90, 120 s
	13 A	30, 60, 90, 120 s
	15 A	30 s
Dilatometry sintering	1450 °C	0 min
	1250 °C	120 min

2.3. Microstructure Characterization

To investigate the microstructure, the cross sections of the pellet-shaped samples were polished and thermally etched at temperatures of around 150 °C lower than the corresponding sintering temperatures for 30 min. The sintering temperatures at the center of the pellet samples were determined by finite element simulations. Subsequently, a gold layer was sputtered on the polished surface using a sputter coaster (Bal-Tec SCD 050, USA), and the microstructure at the center of the cross section of each sample was analyzed by the scanning electron microscopy (SEM) in a Helios Nanolab G3 CX dual-beam focused ion beam (FIB)–SEM (Thermo Fisher Scientific, USA). To determine the average grain size, the linear intercept method was adopted using "Lince-Linear Intercept 2.4.2" software (Nichtmetallisch anorganische Werkstoffe, FB 11, TU Darmstadt, Germany). The grain sizes were measured and calculated according to the standard DIN EN ISO 13383-1 with a conversion factor of 1.56.[38]

3. Numerical Modeling

3.1. Finite Element Modeling

To study the influence of the sintering temperature and the heating rate on the densification, the exact thermal profile of the sample is required. As it is experimentally unrealistic to record the temperature evolution during UHS, it is essential to use FEM modeling to predict the temperature distribution and thermal history of the 8YSZ sample. To this end, a coupled thermal–electrical–structural model was built in the commercial FEM software ABAQUS/Standard (v14, Simulia, Dassault Systèmes) in this work. The UHS setup of copper electrodes, carbon felt, and 8YSZ pellet sample was modeled. The temperatures were calculated based on the self-integrated balance equations[39,40] in ABAQUS, which consider the heat generation induced by Joule heating and the heat transfer by conduction, convection, and radiation. To predict the densification and grain growth during UHS, a constitutive model incorporated with a grain growth law was implemented in a user subroutine UMAT of ABAQUS.

Material properties of 8YSZ, such as thermal conductivity, thermal expansion coefficient, specific heat capacity, Young's modulus, and Poisson's ratio, were adopted from the recent work.[37] The thermal and electrical properties of carbon felt and copper electrodes were obtained as described in the previous work on UHS of STO.[26] To simulate the UHS process, a surface current density was defined on one side of the electrode-felt contact surface, while the other side was defined with a boundary condition of the electrical potential of 0 V. In addition, the surface radiation and the heat conduction of the carbon felt were also considered as boundary conditions. A heat transfer coefficient of 70 W m^{-2} K^{-1} adopted in the model was obtained by a calibration process that compares the simulated surface temperatures with that experimentally measured from the pyrometer. During UHS, the carbon felt was stretched out before it was tightly fixed by two copper electrodes with the screws. In this way, a very good contact was ensured both for the electrode-felt and the felt-sample contact surfaces. Therefore, the thermal contact resistance was insignificant, and thus neglected in the model.

The experimental setup and the simulation model are shown in Figure 1.

3.2. Constitutive Model

In this study, a continuum mechanics (CM) model combined with a grain growth law was employed for the prediction of the densification and grain growth during UHS. One of the most widely used CM models is the Skorohod–Olevsky viscous sintering (SOVS) model,[41,42] which considers a porous body as a two-phase material including a porous body skeleton phase and a void phase. The sintering stress in the constitutive model can be expressed as a function of grain size and density. In this work, Shinagawa's modification was adopted to the SOVS model, in which the constitutive equation for inelastic strain rate is formulated as follows[43,44]

$$\dot{\varepsilon}_{ij} = \frac{1}{2\eta}\frac{1}{\rho^{2n-1}}\left[\sigma'_{ij} + \delta_{ij}\frac{2}{9f^2}(\sigma_m + \sigma_s)\right] \tag{1}$$

$$\sigma_s = \frac{4\gamma}{\xi G}\rho^{N_s}\left[\frac{\rho(1-\rho_0)}{\rho_0(1-\rho)}\right]^{\frac{1}{3}} \tag{2}$$

where η is the shear viscosity of the fully dense material; n is the exponential constant; $f = 1/(2.5\sqrt{1-\rho})$; and σ'_{ij}, σ_m, σ_s represent the deviatoric stress tensor, the hydrostatic stress, and the sintering stress, respectively. δ_{ij} is the Kronecker delta, γ is the specific surface energy, ξ is the correction factor for sintering stress, G is the grain size, N_s is the fitting constant, and ρ_0 is the initial RD. The viscosity η is formulated as an Arrhenius-type function with temperature dependency[45]

$$\eta = C_{s1}T\exp\left(\frac{C_{s2}}{T}\right) \tag{3}$$

where T is the temperature; C_{s1} and C_{s2} are material constants for viscosity. C_{s2} can be expressed as a function of apparent activation energy for material transport resulting in densification Q_d and is given by $C_{s2} = Q_d/R$, where R is the molar gas constant.

According to mass conservation, the rate of density change, $\dot{\rho}$, is defined by the trace of the strain rate tensor, $\dot{\varepsilon}_{kk}$, as follows

$$\dot{\rho} = -\rho \cdot \dot{\varepsilon}_{kk} \tag{4}$$

The constitutive equations indicate that the grain growth during sintering affects the sintering stress, and thus influences the final density. Therefore, a grain growth law is utilized and described by the following equation[46,47]

$$G^p - G_0^p = Kt = K_0 t\exp\left(-\frac{Q_g}{RT}\right) \tag{5}$$

where K_0 is the pre-exponential constant, Q_g is the activation energy for grain growth, and p is the grain growth exponent. Both the constitutive equations and the grain growth law were implemented in the user subroutine UMAT of ABAQUS to predict the densification and grain growth during UHS process.

4. Results and Discussion

4.1. Temperature Distribution during UHS

The simulation result of the temperature distribution in the UHS setup at 13 A for 30 s is shown in **Figure 2**a. The cross section of the carbon felt reveals a large temperature gradient from the surface to the core of the felt, while along the path of the current, the gradient between the two electrodes is small. Additionally, the stabilized temperatures at different currents are demonstrated in Figure 2b, where the blue dots and the blue triangles indicate the temperature on the top surface of the carbon felt from the simulations and the experiments, respectively, and the red dots are the simulated sample temperatures averaged over the whole pellet. It can be seen that the simulated surface temperatures match closely with the temperatures measured by the pyrometer. However, the sample temperatures are much higher than the surface temperatures of the carbon felt. The validation of the temperature simulation for the inner surface of the carbon felt was reported elsewhere.[26]

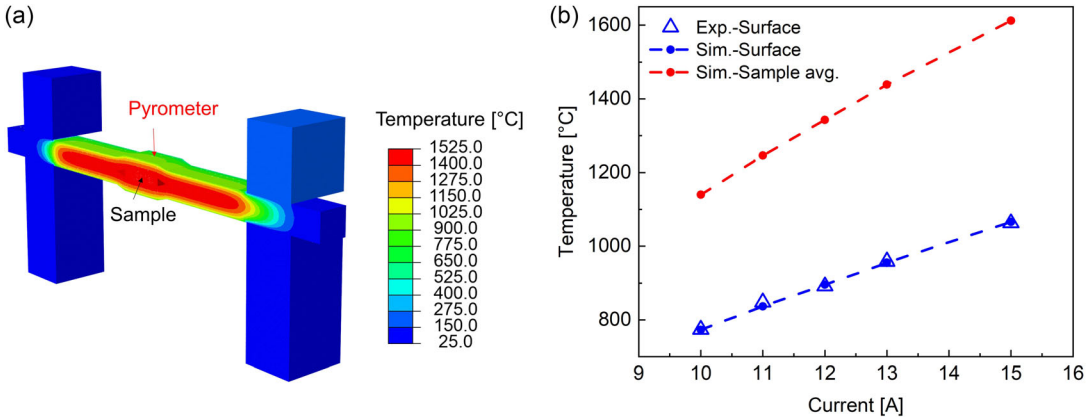

Figure 2. a) Simulated temperature gradient in the UHS setup at the maximum current of 13 A for 30 s, cut along the length of the carbon felt at the half-width position. b) Experimental and simulation results of the stabilized temperatures on the surface of the carbon felt and those of the sample at different maximum currents.

4.2. Densification during UHS

In this study, the interrupted isothermal UHS experiments with the dwell times up to 2 min were conducted to obtain the modeling parameters. The RD of the pellet samples were measured after the sintering experiments, and the results are given in **Figure 3**. It shows that for a dwell time above 1 min, an almost full densification (RD > 97%) can be achieved at the maximum current of 13 A, which corresponds to a simulated average sample temperature of 1439 °C. At the maximum current of 15 A, 8YSZ sample can be densified in 30 s. For comparison, dilatometry sintering experiments with a heating rate of 5 K min^{-1} were carried out on 8YSZ samples in argon. The results show that a RD of ≈95% of the 8YSZ sample can be achieved by sintering at 1450 °C with no holding time. This is similar to the sample temperature at the maximum current of 13 A during UHS, although much longer total processing time was needed for CS (≈10 h) compared to UHS (< 20 min). It is worth noting that most of the processing time of UHS is for evacuation and filling the chamber with argon (≈16 min). Full cycle time could be reduced to a few minutes by using a stronger vacuum pump and a higher argon flow rate. From the comparison of UHS and CS, it can be concluded that no extremely high sample temperature played a role in the densification of 8YSZ during UHS. As the samples were heated only by thermal conduction and radiation, the influence of electric field can also be excluded. Hence, the ultrahigh heating rate seems to be the dominant factor that enhances densification. The influence of heating rate on densification will be discussed in later chapters.

The modeling parameters were determined by the linear regression plots. The detailed identification process was explained in the previous work on FS.[37] The same strategy was adopted for the modeling of UHS in this study. The activation energies for the densification Q_d and for the grain growth Q_g were calculated to be 246 and 405 kJ mol^{-1}. With the determined model parameters, the densification during UHS was simulated and the comparisons of numerical and experimental results are summarized in **Table 2**.

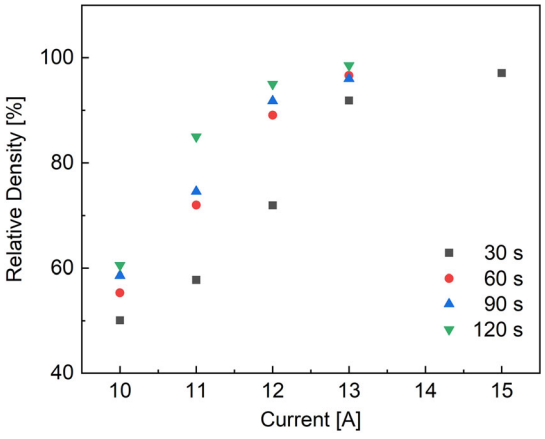

Figure 3. Experimental results of RD of UHS sintered samples at different maximum currents and dwell times. Presintered green bodies had a RD of 45% ± 2%.

Table 2. Comparison of simulation and experimental results of densification.

Current [A]	Relative density [%]					
	60 [s]		90 [s]		120 [s]	
	Exp.	Sim.	Exp.	Sim.	Exp.	Sim.
10	55.3	50.4	58.6	58.0	60.5	65.5
11	72.0	60.4	74.6	75.7	85.0	86.0
12	89.1	75.8	91.8	89.6	95.0	96.4
13	96.6	85.3	96.0	95.7	98.6	99.6

The table shows a good agreement between the numerical and experimental results for the UHS sintered samples with long dwell times (>60 s), whereas for the short dwell times (≤60 s), an underestimation of the simulation results was observed. The reason for the deviation of the simulation results with short dwell times could be attributed to the inaccuracy of the simulated heat-up time. The heat-up time denotes the time needed for the 8YSZ sample to reach its highest temperature and stabilize. Unlike the carbon felt, of which the temperature peaks in 3 s,[26] the 8YSZ sample generally takes 30–40 s to reach its highest temperature based on the simulation results. However, the temperature simulation was first carried out without considering the shrinkage of the sample, which could lead to an imprecise prediction of the temperature evolution before the maximum value is reached. In reality, the sample could already reach the highest temperature before the simulated peak time; thus, the real densities of the samples with short dwell times are higher than simulated values. With the increase of the dwell time, the impact of this model deficiency becomes smaller, as the stabilized highest temperatures were relatively accurately predicted.[26]

In **Figure 4**, the UHS sintered samples at 11 A for 120 s and 13 A for 120 s are demonstrated. Their simulated density and temperature distributions are shown alongside. The blackening of the sample surface after UHS was resulted from the carbothermal reduction.[21,48] With a higher current level, the blackening is more evident. However, this only occurs on the surface of the pellet sample and can be removed easily by grinding. Moreover, after sintering at 11 A, it was found that the diameter of the real sample along the *x*-axis, where the current flows through the carbon felt, is smaller than that along the *z*-axis. This irregular shape of the pellet sample can be explained by the inhomogeneity of the density and temperature distribution shown in Figure 4, where the density and temperature along the diameter aligned with the *z*-axis are smaller than that aligned with the *x*-axis. Thus, the shrinkage along the diameter aligned with the *z*-axis is smaller than that aligned with the *x*-axis. This density gradient decreases with increasing maximum current during UHS. As can be seen in the figure, the density gradient in the sample of 13 A is much smaller than that of 11 A. However, the temperature gradient remains distinct even at high maximum currents. The temperature inhomogeneity is induced by the rapid heat dissipation to the environment through conduction and radiation, therefore, can be suppressed by a thermal insulator.[9] Additionally, the simulation results reveal that the largest heat dissipation appears at the ends of the pellet sample

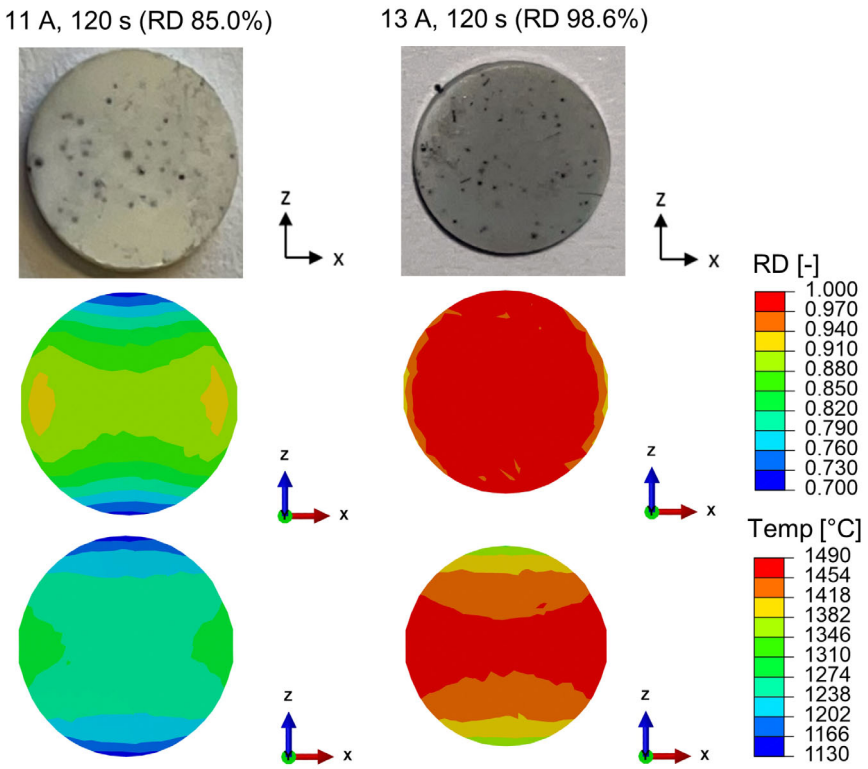

Figure 4. Optical image (up), simulation of RD distribution (middle), and simulation of temperature distribution (down) of UHS sintered samples at 11 A for 120 s (left) and 13 A for 120 s (right).

close to the opening of the carbon felt. Hence, the temperature gradient can be mitigated by increasing the width of the carbon felt. The downside of a wider carbon felt is that the current density decreases proportionally. In future works, FEM modeling can be used to guide the modification of the experimental setup in two ways to achieve a more homogenous sample temperature: on the one hand, different widths and shapes of the carbon felt as well as the sample can be adjusted to find a criterion, for instance, a critical ratio of the sample width to the carbon felt width, at which the sample can be densified at an affordable energy expense with the minimum temperature gradient. On the other hand, the current profile can be modified (e.g., a stepwise mode) in the model to allow a gradual increment in the temperature, which can also decrease the temperature gradient in the sample. This numerical strategy has significant potential to reduce the thermal stress in the sample, and thus prevent cracking when scaling up the sample size.

4.3. Grain Growth during UHS

Figure 5 shows the microstructures at the center of the polished and etched cross sections of the UHS sintered samples at different currents with 120 s. The SEM micrographs indicate that the average grain size of the 8YSZ sample increases with increasing current for the same dwell time. Moreover, the grain continues to grow with increasing dwell time, as shown in the experimental results of **Figure 6**a. At 13 A for 120 s, the sample was almost

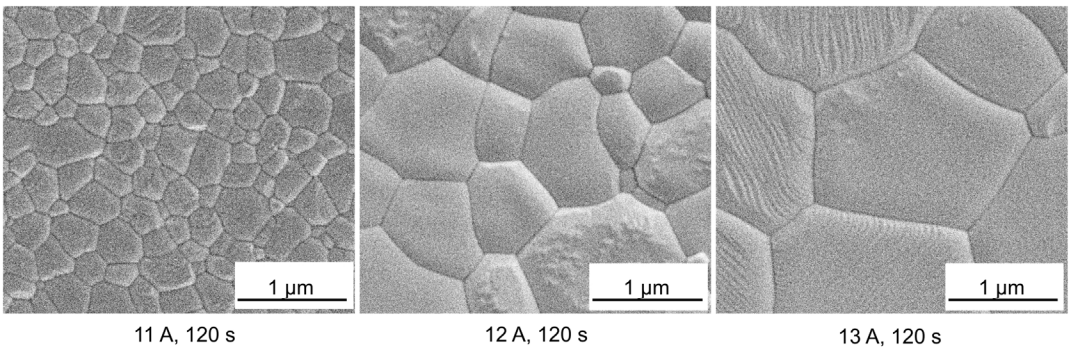

Figure 5. SEM micrographs of the UHS sintered 8YSZ samples at the maximum currents of 11, 12, and 13 A for 120 s in argon atmosphere.

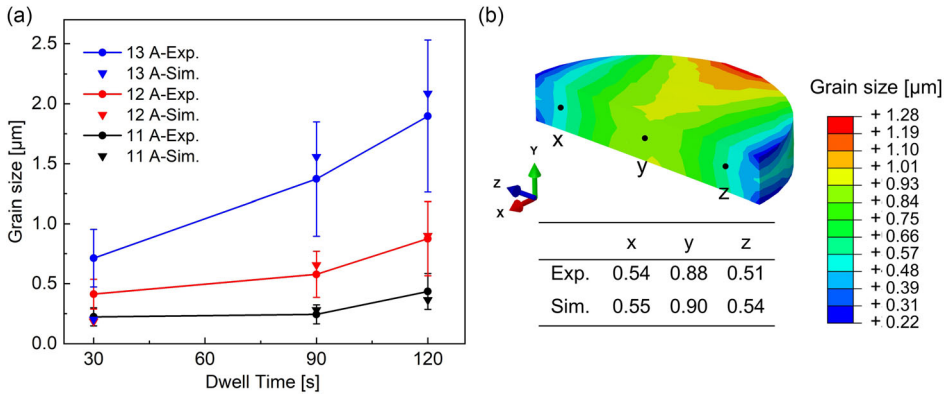

Figure 6. a) Comparison of simulation and experimental results of grain sizes of UHS sintered samples at 11, 12, and 13 A. b) Simulation result of grain size distribution in the UHS sintered sample at 12 A for 120 s and the comparison between experimental and simulation results of the grain size at the position *x*, *y*, and *z*.

fully densified with a grain size of 1.9 μm, which is comparable to the grain size of the conventionally sintered 8YSZ samples. The grain growth behavior during UHS reveals that the rapid densification is unlikely due to a fine-grained microstructure caused by the ultrahigh heating rate.

Figure 6a compares the experimental and numerical results of the grain size evolutions with respect to the dwell time at different maximum currents. A good agreement between the experimental and numerical values is achieved with long dwell times (>60 s); with the dwell time of 30 s, simulation results show an underestimation of the real grain sizes. This inaccurate prediction corresponds to the simulation results of the densification and can be explained by the imprecise prediction of the heat-up time during UHS.

Figure 6b demonstrates the grain size distribution in the sample that was sintered by UHS at 12 A for 120 s. This grain size inhomogeneity is caused by the temperature gradient in the pellet-shaped sample. To verify the simulated grain size gradient, three different locations, corresponding to the marked *x*, *y*, and *z* in the graph, on the cross section of the half of the experimentally produced pellet sample, were observed in the SEM. The grain sizes of the three positions were measured and compared to the simulation results, as shown in the inset table of Figure 6b. It can be seen that the center of the cross section (position *y*) has the largest grain size, whereas the grain sizes at the two sides (*x* and *z*) are smaller than the center and similar to each other. This symmetrical grain size distribution was accurately predicted by the simulation.

4.4. Comparison of UHS and FS

UHS and FS have similar heating rates and both can densify ceramic materials within tens of seconds. The difference between the two techniques lies in the heating method of the sample. In UHS, the sample is heated through thermal radiation and conduction (indirectly by the electric field), whereas in FS the current flows through the green body and the sample is heated by Joule heating induced directly by the electric field. Therefore, to investigate the role of heating rate and electric field on the sintering behavior of 8YSZ, it is essential to compare UHS and FS regarding the densification and grain growth behaviors.

The sintering trajectories of the 8YSZ samples for FS, UHS, and CS are plotted in **Figure 7**. The grain sizes were measured in the center of the samples for FS, UHS, and CS to exclude the

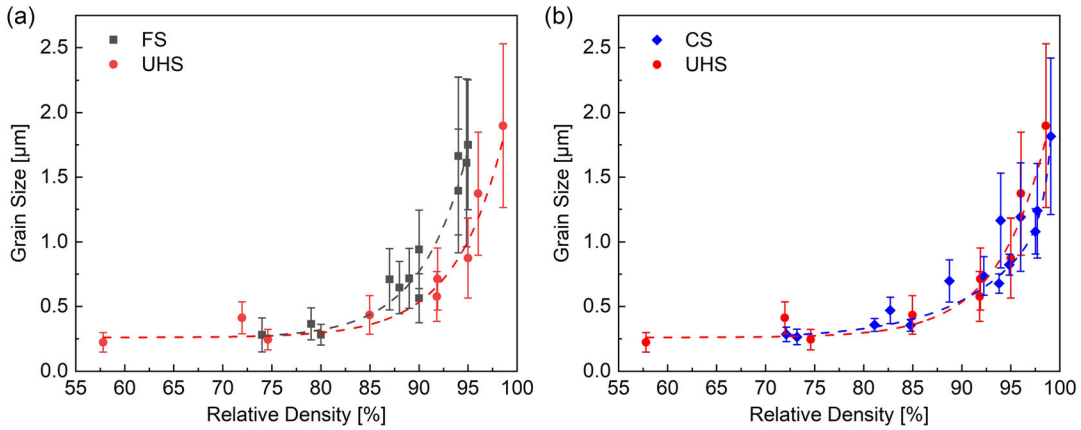

Figure 7. Comparison of sintering trajectory of 8YSZ: a) flash sintered in air and UHS sintered in argon; b) conventionally sintered in air and UHS sintered in argon.

effect of electrical polarity. The values of RD are averages of the whole sample/gauge section. It can be seen from Figure 7b that the trajectories of CS and UHS align well with each other. However, a slight difference in the slope of the trajectory between FS and UHS can be observed in Figure 7a. At the RD above 85%, the slope of the trajectory for FS is higher than that for UHS. The larger slope indicates an early start of the grain growth during sintering, and thus a more evident grain coarsening and limited densification. However, the difference between the two trajectories is not evident and could be caused by measurement errors. This difference can, nevertheless, be explained by the final density of the sintered samples: the largest RD achieved in 8YSZ of UHS is 98.6%, whereas that for FS is only 95%. The possible influencing factors for the sintering trajectory are heating rate, atmosphere, and electric field. According to the temperature simulation, the average heating rate of UHS experiments of 8YSZ does not exceed that of FS. Therefore, the less grain coarsening in UHS cannot be explained by the suppression of grain growth due to a higher heating rate. The sintering atmosphere was also reported to influence the sintering behavior of ceramic materials.[49–52] Yan et al.[50] found that a reducing atmosphere produces a large grain size of $BaTiO_3$. Additionally, it was observed that the grain boundary mobility of Fe_3O_4 was inversely proportional to the square root of the partial pressure of O_2. Ubenthiran et al.[36] have sintered 3YSZ both in air and argon atmosphere. It was discovered that the grain sizes of the samples sintered in argon are smaller than that in air with the same sintering temperatures. Moreover, the densities achieved in argon were also smaller than that in air. When a sintering trajectory is constructed from the work of Ubenthiran, it can be seen that the atmosphere does not influence the trajectory much. In this work, UHS experiments were conducted in argon, which is an oxygen-deficient environment. Based on the discussion above, the atmosphere is not able to explain the smaller grain size in UHS compared to FS either. Therefore, it can be concluded that the different sintering behavior is most plausibly due to the impact of the electric field, which was applied to the sample in FS and absent in UHS. Electric field has been reported to be able to redistribute point defects and change the grain boundary mobility at the electrode sides during FS.[53,54] As the current work analyzed the microstructure at the middle of the sample, it is plausible to say that the defect redistribution could occur over the entire sample during FS under the effect the electric field.

In the previous work on FS of 8YSZ,[37] CS and FS were compared at similar sintering temperatures to study the influence of the heating rate. The results are again shown here in **Table 3**. In this study, the conventional dilatometry sintering experiments were conducted on 8YSZ in argon to compare with UHS. The densification curves were converted from the shrinkage curves obtained from the dilatometer experiments. Different temperatures and holding times were chosen for comparison, and the corresponding densities were read from the densification curves. The results are summarized in **Table 4**. It is important to note that the dwell times of UHS in the table are the real dwell times of the samples instead of the set dwell times of the experimental procedure. Considering the heat-up times of the samples before their highest temperatures were reached, the real dwell times were obtained by subtracting the heat-up times from the set dwell times during the experiments. The heat-up time was assumed to be 30 s during UHS based on the simulation results.

Table 3. Comparison of CS and FS at similar temperatures in air.[37]

CS (air)				FS (air)			
Temp. [°C]	Dwell time [s]	Heating rate [K min^{-1}]	RD [%]	Temp. [°C]	Dwell time [s]	Heating rate [K min^{-1}]	RD [%]
1200	60	5	52.9	1171	15	3012	72.6
1300	60	5	71.7	1294	30	2892	86.6
1350	120	5	88.7	1326	120	1393	93.7

Table 4. Comparison of CS and UHS at similar temperatures in argon.

CS (argon)				UHS (argon)			
Temp. [°C]	Dwell time [s]	Heating rate [K min^{-1}]	RD [%]	Temp. [°C]	Dwell time[a)] [s]	Heating rate [K min^{-1}]	RD [%]
1102	0	5	45.3	1102	0	2573	57.8
1224	0	5	51.4	1224	0	2759	72.0
1335	0	5	71.9	1335	0	2976	91.9
1250	7200	5	77.8	1246	90	2573	85.0

[a)]The dwell times of UHS denote to the real dwell time of the samples.

Table 3 shows that at similar sintering temperatures, FS can achieve higher densification than CS with a shorter holding time. The significantly higher heating rate of FS is believed to be responsible for the enhanced densification. However, the role of electric field cannot be completely excluded with respect to the previous study. Table 4 reveals that pronounced increases in the RD can be achieved by UHS at the same temperatures with the same or shorter holding times compared with the CS. By comparing the conclusions drawn from Table 3 and 4, it is clear that our results support the correctness of the theory of heating rate effect: the enhanced densification during both FS and UHS is caused by the ultrahigh heating rate, which is in accordance with fundamental works of Harmer et al.[55] from the early 1980s, while the influence of electric field in FS is mostly on the grain growth. Furthermore, by comparing the CS of 8YSZ in air and in argon, it can also be concluded that the 8YSZ samples are more easily densified in air than in argon.

From the determined constitutive models, the activation energy for densification of 8YSZ during UHS is 246 kJ mol^{-1}, which is much smaller than those of the CS (691 kJ mol^{-1}) and the FS (424 kJ mol^{-1}) carried out in air.[37] As UHS experiments were conducted in argon, a direct comparison is hard to perform considering the effect of sintering atmosphere. However, experiments show that at the same temperature, the 8YSZ samples were more densified in air than in argon. This indicates a higher activation energy than 691 kJ mol^{-1} for CS in argon. Hence, a conclusion can be made that UHS substantially decreases the apparent activation energy for densification of 8YSZ. This observation also corresponds to the previous studies.[18,21] The change in the apparent activation energy of densification can be correlated to the altered dominant mass transport mechanism during sintering. It is known[56,57] that the grain boundary diffusion is the predominant initial

sintering mechanism for matter transport in yttria-stabilized zirconia, which is associated with an activation energy of 702–716 kJ mol^{-1} for CS of 8YSZ.[58,59] The values are close to those in our previous study on CS of 8YSZ (691 kJ mol^{-1}). The activation energy of lattice diffusion of 8YSZ varies between 223 and 460 kJ mol^{-1} in the literature,[60–62] which corresponds to our results of UHS (246 kJ mol^{-1}) and FS (424 kJ mol^{-1}). Therefore, it is likely that the sintering technique with high heating rate (UHS and FS) changes the dominant mass transport mechanism of 8YSZ from grain boundary diffusion to lattice diffusion. This conclusion is also consistent with the work of Suárez et al.,[62] where the sintering mechanism of 8YSZ at a fast heating rate (400–600 K min^{-1}) is found to be dominated by volume diffusion (lattice diffusion). However, a large discrepancy exists in the literature on the activation energy of 8YSZ. For example, a much lower activation energy (309 kJ mol^{-1}) for grain boundary diffusion than 702 kJ mol^{-1} has also been reported for 8YSZ.[61] The reason for the contradictory values could be attributed to the different experimental methods, particle sizes, initial densities, and temperature ranges applied. On the other hand, the sintering process is normally not dominated by a single mechanism. In a practical case, various sintering mechanisms often operate simultaneously. Thus, it is not easy to assign each sintering technique to a single sintering mechanism based on the calculated activation energies. In addition to grain boundary diffusion and lattice diffusion, the densification-noncontributing surface diffusion is believed to increase the apparent activation energy for densification.[63] As high heating rate can suppress surface diffusion in the low-temperature range during UHS, a decrease in the activation energy of densification during UHS is expected.

5. Summaries

In this study, a novel UHS has been successfully applied to fully consolidate 8YSZ material within 30 s. The densification and grain growth of 8YSZ during UHS were investigated both experimentally and numerically. The results were compared with FS of the 8YSZ to study the role of the heating rate on ECAS. The following conclusions can be drawn from this work: 1) The 8YSZ samples can achieve almost full densification by UHS in argon at 15 A for 30 s, or at 13 A for 60 s. The maximum current of 13 A corresponds to the highest average sample temperature of 1439 °C, which is comparable to the sintering temperature of 8YSZ in conventional furnaces. 2) The RD and grain size prediction from the FEM match closely with the experimental observation for long dwell times ($>$ 60 s), but do not match well for short dwell times ($<$ 60 s). The grain size inhomogeneity was successfully predicted for the UHS sintered sample at 12 A for 120 s. The results agree well with the experimental values. 3) The slope of the sintering trajectory of the FS of the 8YSZ is a little bit larger than that of UHS. This indicates a more evident grain coarsening and limited densification for FS due to the effect of electric field. 4) UHS can make 8YSZ samples reach a higher density with the same sintering temperatures and the same/shorter dwell times compared with CS. The enhanced densification during both UHS and FS can be contributed mainly to the ultrahigh heating rate. 5) The apparent activation energy for densification of the 8YSZ during UHS is 246 kJ mol^{-1}, which is smaller than those of CS and FS. The decrease in activation energy could be attributed to the altered dominant mass transport mechanism and the suppression of surface diffusion by the ultrahigh heating rate of UHS.

Acknowledgements

This study was funded by the Deutsche Forschungsgemeinschaft (DFG, German Research Foundation) under the Priority Programme (SPP) 1959/2 [319257740], [BR 1844/21-2], and [BR 3418/1-2], which is highly acknowledged.

Open Access funding enabled and organized by Projekt DEAL.

Conflict of Interest

The authors declare no conflict of interest.

Data Availability Statement

The data that support the findings of this study are available from the corresponding author upon reasonable request.

Keywords

8 mol% Y2O3-stabilized ZrO2 (8YSZ), electric current-assisted sintering (ECAS), finite element modeling (FEM), flash sintering, heating rates, ultrafast high-temperature sintering (UHS)

Received: January 31, 2023
Revised: February 27, 2023
Published online:

[1] R. M. German, *Sintering: From Empirical Observations to Scientific Principles* **2014**, 305, https://doi.org/10.1016/B978-0-12-401682-8.00010-0.
[2] H. V. Atkinson, S. Davies, *Metall. Mater. Trans. A* **2000**, *31*, 2981.
[3] *Ceramic Processing and Sintering* (Ed: M. N. Rahaman), Marcel Dekker, New York **2003**.
[4] K. Watari, H. J. Hwang, M. Toriyama, S. Kanzaki, *J. Mater. Res.* **1999**, *14*, 1409.
[5] K. Nur, T. P. Mishra, J. G. P. Da Silva, J. Gonzalez-Julian, M. Bram, O. Guillon, *J. Eur. Ceram. Soc.* **2021**, *41*, 2648.
[6] M. Biesuz, V. M. Sglavo, *J. Eur. Ceram. Soc.* **2019**, *39*, 115.
[7] T. P. Mishra, R. R. I. Neto, R. Raj, O. Guillon, M. Bram, *Acta Mater.* **2020**, *189*, 145.
[8] M. Kermani, J. Dong, M. Biesuz, Y. Linx, H. Deng, V. M. Sglavo, M. J. Reece, C. Hu, S. Grasso, *J. Eur. Ceram. Soc.* **2021**, *41*, 6626.
[9] J. Dong, V. Pouchly, M. Biesuz, V. Tyrpekl, M. Vilémová, M. Kermani, M. Reece, C. Hu, S. Grasso, *Scr. Mater.* **2021**, *203*, 114076.
[10] A. Krell, P. Blank, H. Ma, T. Hutzler, M. P. B. Bruggen, R. Apetz, *J. Am. Ceram. Soc.* **2003**, *86*, 12.
[11] S. Grasso, Y. Sakka, G. Maizza, *Sci. Technol. Adv. Mater.* **2009**, *10*, 53001.
[12] E. Zapata-Solvas, D. Gómez-García, A. Domínguez-Rodríguez, R. I. Todd, *Sci. Rep.* **2015**, *5*, 8513.
[13] M. Bram, A. M. Laptev, T. P. Mishra, K. Nur, M. Kindelmann, M. Ihrig, J. G. Da Pereira Silva, R. Steinert, H. P. Buchkremer, A. Litnovsky,

F. Klein, J. Gonzalez-Julian, O. Guillon, *Adv. Eng. Mater.* **2020**, *22*, 2000051.
[14] O. Guillon, J. Gonzalez-Julian, B. Dargatz, T. Kessel, G. Schierning, J. Räthel, M. Herrmann, *Adv. Eng. Mater.* **2014**, *16*, 830.
[15] Z. A. Munir, U. Anselmi-Tamburini, M. Ohyanagi, *J. Mater. Sci.* **2006**, *41*, 763.
[16] M. Cologna, B. Rashkova, R. Raj, *J. Am. Ceram. Soc.* **2010**, *93*, 3556.
[17] R. Raj, M. Cologna, A. L. G. Prette, V. Sglavo, *Methods of Flash Sintering* **2013**, https://www.google.com/patents/US20130085055.
[18] C. Wang, W. Ping, Q. Bai, H. Cui, R. Hensleigh, R. Wang, A. H. Brozena, Z. Xu, J. Dai, Y. Pei, C. Zheng, G. Pastel, J. Gao, X. Wang, H. Wang, J.-C. Zhao, B. Yang, X. R. Zheng, J. Luo, Y. Mo, B. Dunn, L. Hu, *Science* **2020**, *368*, 521.
[19] M. Biesuz, A. Galotta, A. Motta, M. Kermani, S. Grasso, J. Vontorová, V. Tyrpekl, M. Vilémová, V. M. Sglavo, *Mater. Sci. Eng., C* **2021**, *127*, 112246.
[20] R.-F. Guo, H.-R. Mao, Z.-T. Zhao, P. Shen, *Scr. Mater.* **2021**, *193*, 103.
[21] Y. Lin, N. Luo, E. Quattrocchi, F. Ciucci, J. Wu, M. Kermani, J. Dong, C. Hu, S. Grasso, *Ceram. Int.* **2021**, *47*, 21982.
[22] *Ultra-Rapid Sintering: Volume 16 Sintering and Heterogeneous Catalysis* (Ed: D. L. Johnson), Springer US, Boston, MA **1984**.
[23] D. L. Johnson, *J. Am. Ceram. Soc.* **1990**, *73*, 2576.
[24] M.-Y. Chu, M. N. Rahaman, L. C. Jonghe, R. J. Brook, *J. Am. Ceram. Soc.* **1991**, *74*, 1217.
[25] W. Ji, B. Parker, S. Falco, J. Y. Zhang, Z. Y. Fu, R. I. Todd, *J. Eur. Ceram. Soc.* **2017**, *37*, 2547.
[26] T. P. Mishra, S. Wang, C. Lenser, D. Jennings, M. Kindelmann, W. Rheinheimer, C. Broeckmann, M. Bram, O. Guillon, *Acta Mater.* **2022**, *231*, 117918.
[27] Y. Zhang, J. Nie, J. M. Chan, J. Luo, *Acta Mater.* **2017**, *125*, 465.
[28] W. Ji, J. Zhang, W. Wang, Z. Fu, R. I. Todd, *J. Eur. Ceram. Soc.* **2020**, *40*, 5829.
[29] C. Schmerbauch, J. Gonzalez-Julian, R. Röder, C. Ronning, O. Guillon, *J. Am. Ceram. Soc.* **2014**, *97*, 1728.
[30] W. Xu, A. Maksymenko, S. Hasan, J. J. Meléndez, E. Olevsky, *Acta Mater.* **2021**, *206*, 116596.
[31] Y. Li, R. Torchio, S. Falco, P. Alotto, Z. Huang, R. I. Todd, *J. Eur. Ceram. Soc.* **2021**, *41*, 6649.
[32] K. S. Arya, A. Eqbal, P. Rai, D. Yadav, T. Chakrabarti, *J. Am. Ceram. Soc.* **2022**, *105*, 6049.
[33] S. Grasso, Y. Sakka, N. Rendtorff, C. Hu, G. Maizza, H. Borodianska, O. Vasylkiv, *J. Ceram. Soc. Jpn.* **2011**, *119*, 144.
[34] J. G. Pereira da Silva, J.-M. Lebrun, H. A. Al-Qureshi, R. Janssen, R. Raj, *J. Am. Ceram. Soc.* **2015**, *98*, 3525.
[35] R.-X. Luo, M. Kermani, Z.-L. Guo, J. Dong, C.-F. Hu, F. Zuo, S. Grasso, B.-B. Jiang, G.-L. Nie, Z.-Q. Yan, Q. Wang, Y.-L. Gan, F.-P. He, H.-T. Lin, *J. Eur. Ceram. Soc.* **2021**, *41*, 6338.
[36] S. Ubenthiran, M. Thanihaichelvan, R. Singh, *J. Mater. Eng. Perform.* **2018**, *27*, 3574.
[37] S. Wang, T. P. Mishra, Y. Deng, A. Kaletsch, M. Bram, C. Broeckmann, *Adv. Eng. Mater.* **2023**, 2201744.
[38] M. I. Mendelson, *J. Am. Ceram. Soc.* **1969**, *52*, 443.
[39] Hibbitt, Karlsson, Sorensen, *ABAQUS 5.8 Theory Manual*, Hibbitt, Karlsson & Sorensen Inc, Pawtucket, USA **1998**.
[40] A. Zavaliangos, J. Zhang, M. Krammer, J. R. Groza, *Mater. Sci. Eng., A* **2004**, *379*, 218.
[41] V. V. Skorohod, *Rheological Basis of the Theory of Sintering*, Naukova Dumka, Kiev **1972**.
[42] E. A. Olevsky, *Mater. Sci. Eng., R* **1998**, *23*, 41.
[43] K. Shinagawa, *Comput. Mater. Sci.* **1999**, *13*, 276.
[44] K. Shinagawa, *JSME Int. J., Ser. A* **1996**, *39*, 565.
[45] M. W. Reiterer, K. G. Ewsuk, J. G. Arguello, *J. Am. Ceram. Soc.* **2006**, *89*, 1930.
[46] J. E. Burke, D. Turnbull, *Prog. Met. Phys.* **1952**, *3*, 220.
[47] M. Hillert, *Acta Metall.* **1965**, *13*, 227.
[48] J. Wu, M. Kermani, D. Zhu, J. Li, Y. Lin, C. Hu, S. Grasso, *Scr. Mater.* **2022**, *210*, 114476.
[49] T. K. Gupta, R. L. Coble, *J. Am. Ceram. Soc.* **1968**, *51*, 521.
[50] M. F. Yan, *Mater. Sci. Eng.* **1981**, *48*, 53.
[51] P.-L. Chen, I.-W. Chen, *J. Am. Ceram. Soc.* **1994**, *77*, 2289.
[52] A. Kabir, H. Zhang, V. Esposito, *Cerium Oxide (CeO_2): Synthesis, Properties and Applications*, Elsevier **2020**, p. 169, https://doi.org/10.1016/B978-0-12-815661-2.00005-0.
[53] W. Rheinheimer, J. P. Parras, J.-H. Preusker, R. A. de Souza, M. J. Hoffmann, *J. Am. Ceram. Soc.* **2019**, *102*, 3779.
[54] Y. Zhang, J.-I. Jung, J. Luo, *Acta Mater.* **2015**, *94*, 87.
[55] M. P. Harmer, R. J. Brook, *J. Br. Ceram. Soc.* **1981**, *5*, 147.
[56] W. S. Young, I. B. Cutler, *J. Am. Ceram. Soc.* **1970**, *53*, 659.
[57] K. Matsui, N. Ohmichi, M. Ohgai, T. Yamakawa, M. Uehara, N. Enomoto, J. Hojo, *J. Ceram. Soc. Jpn. Suppl.* **2004**, *112*, S343.
[58] K. Matsui, K. Tanaka, N. Enomoto, J. Hojo, *J. Ceram. Soc. Jpn.* **2006**, *114*, 763.
[59] G. Suárez, Y. Sakka, *Ceram. Int.* **2010**, *36*, 879.
[60] R. L. González-Romero, J. J. Meléndez, D. Gómez-García, F. L. Cumbrera, A. Domínguez-Rodríguez, F. Wakai, *Solid State Ionics* **2011**, *204–205*, 1.
[61] A. H. Chokshi, *Scr. Mater.* **2003**, *48*, 791.
[62] G. Suárez, L. B. Garrido, E. F. Aglietti, *Mater. Chem. Phys.* **2008**, *110*, 370.
[63] G. Sethi, S. J. Park, J. L. Johnson, R. M. German, *Int. J. Refract. Met. Hard Mater.* **2009**, *27*, 688.